Spin-orbit interaction and anomalous spin relaxation in carbon nanotube quantum dots

Denis V. Bulaev,[1] Björn Trauzettel,[1,2] and Daniel Loss[1]
[1]*Department of Physics, University of Basel, Klingelbergstrasse 82, CH-4056 Basel, Switzerland*
[2]*Institute of Theoretical Physics and Astrophysics, University of Würzburg, D-97074 Würzburg, Germany*
(Received 21 January 2008; published 3 June 2008)

We study spin relaxation and decoherence in nanotube quantum dots caused by electron-lattice and spin-orbit interaction and predict striking effects induced by magnetic fields B. For particular values of B, destructive interference occurs resulting in ultralong spin relaxation times T_1 exceeding tens of seconds. For small phonon frequencies ω, we find a $1/\sqrt{\omega}$ spin-phonon noise spectrum—a dissipation channel for spins in quantum dots—which can reduce T_1 by many orders of magnitude. We show that nanotubes exhibit zero-field level splitting caused by spin-orbit interaction. This enables an all-electrical and phase-coherent control of spin.

DOI: 10.1103/PhysRevB.77.235301 PACS number(s): 72.25.Rb, 85.35.Kt, 63.22.Gh, 75.75.+a

I. INTRODUCTION

Although semiconductor spintronics is a field with already a substantial history as well as with commercial applications,[1] spintronics with carbon-based materials is a young research area with excellent perspectives. Only very recently, a pronounced gate-controlled magnetoresistance response in carbon nanotubes connected to ferromagnetic leads has been reported.[2] Furthermore, spin injection and detection in single-wall carbon nanotubes has been demonstrated using a four-terminal geometry.[3] The interest to implement spintronic devices with carbon materials such as carbon nanotubes[4] or graphene[5] is mainly driven by the desire to improve material properties, for instance, for the spin relaxation behavior in these materials (as compared to more standard semiconductors such as GaAs). This is so because carbon is a comparably light atom; thus, spin-orbit interaction is typically weak.[6] Additionally, it consists predominantly of ^{12}C, which has zero nuclear spin; thus, spin decoherence and relaxation caused by the hyperfine interaction of the electron spin with the surrounding nuclear spins are weak. The advantageous material properties of carbon also trigger a large interest to create spin qubits[7] in such materials.

Here, we provide quantitative calculations of spin relaxation and spin decoherence times and show that they are dominated by a combination of spin-orbit and electron-phonon interaction. It turns out that such spin-orbit induced effects get strongly enhanced in small-radius nanotubes due to the curvature of the lattice and result in energy splittings that even exceed those occurring in GaAs nanostructures.

The interplay of such enhanced spin-orbit interaction with the one-dimensional nature of nanotubes results in a complex behavior with an extremely wide range of relaxation rates which can be varied over many orders of magnitude by an external magnetic field applied along the tube axis. We show that interference effects can result in *ultralong* spin relaxation times exceeding tens of seconds. By contrast, we uncover that for nanotube quantum dots, a spin-phonon dissipation channel exists with a sub-Ohmic spectral function ($\propto 1/\sqrt{\omega}$, see below), which results in *decreasing* spin relaxation times for decreasing spin level splitting ω. Compared to standard quantum dots (such as GaAs or InAs semiconductors), this is a most surprising behavior since usually the spin decay times increase for decreasing ω.[8–10]

Most remarkably, at zero magnetic field, the spin-orbit interaction induces a zero-field splitting in the energy spectrum. We show that this opens the door for an all-electrical control of spin in nanotube quantum dots, again based on the strong spin-orbit interaction. This feature is most interesting for spintronics applications where one aims at a spin manipulation without making use of magnetic fields. Since quantum dots in semiconducting carbon nanotubes have been realized by several groups,[11–18] we believe that our predictions are well within experimental reach.

The paper is organized as follows. In Sec. II, we introduce a theoretical model for a nanotube quantum dot and solve the spectral problem of the Hamiltonian of such a system. In Sec. III, we study spin-orbit coupling in nanotubes, consider different contributions to the spin-orbit coupling, and investigate zero-field-level splitting induced by spin-orbit coupling. In Sec. IV, electron-phonon coupling in nanotubes is considered. Analytical expressions for the coupling of an electron to three deformational acoustic phonon modes are obtained. In Sec. V, spin relaxation of an electron in a nanotube quantum dot is investigated and discussed.

II. THEORETICAL MODEL

We consider a single-wall nanotube (NT) defined by the chiral vector $\mathbf{C}_h = n_1\mathbf{a}_1 + n_2\mathbf{a}_2$, where $\mathbf{a}_1 = a_0(1,0)$ and $\mathbf{a}_2 = a_0(1/2, \sqrt{3}/2)$ are the primitive lattice vectors ($a_0 = 0.246$ nm) and $n_1, n_2 \in \mathbb{Z}$.[4] The indices (n_1, n_2) determine the radius of a NT $R = |\mathbf{C}_h|/2\pi = a_0\sqrt{n_1^2 + n_2^2 + n_1 n_2}/2\pi$ and the chiral angle (direction angle of $\mathbf{C}_h$) $\theta = \arctan[\sqrt{3}n_2/(2n_1 + n_2)]$ (see Fig. 1). Neglecting curvature effects (which lead to an inessential shift of the valley minima in $\mathbf{k}$ space[4]) and spin-orbit interaction (SOI), we describe the system at the $\mathbf{K} = (2\pi/a_0)(1/3, 1/\sqrt{3})$ and the $\mathbf{K}' = (2\pi/a_0)(-1/3, 1/\sqrt{3})$ points of the Brillouin zone (see inset in Fig. 1) by the Hamiltonian of graphene,[19]

$$\tilde{H}_0 = \hbar v(\tau_3 k_x \sigma_1 + k_y \sigma_2) = \hbar v \begin{pmatrix} 0 & (\tau_3\kappa - ik)e^{-i\tau_3\theta} \\ (\tau_3\kappa + ik)e^{i\tau_3\theta} & 0 \end{pmatrix}, \quad (1)$$

where v is the Fermi velocity in a NT ($v = 8.1 \times 10^7$ cm/s),[20]

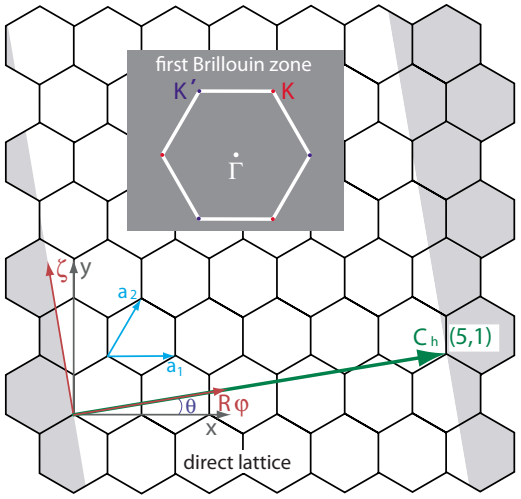

FIG. 1. (Color online) Two-dimensional hexagonal lattice. Here $\mathbf{a}_1$ and $\mathbf{a}_2$ are the primitive lattice vectors, $\mathbf{C}_h=n_1\mathbf{a}_1+n_2\mathbf{a}_2$ is the chiral vector (in this figure, we show the chiral vector with $n_1=5$ and $n_2=1$), θ is the chiral angle, ζ is along the NT axis, and $R\varphi$ is the azimuthal direction of a NT. In gray inset, the first Brillouin zone is depicted, where $\Gamma=(0,0)$ is the center of the zone; $\mathbf{K}$ and $\mathbf{K}'$ are nonequivalent points in the Brillouin zone.

σ_j are Pauli matrices operating on sublattice space, $\tau_3=1$ ($\tau_3=-1$) for the $\mathbf{K}$ ($\mathbf{K}'$) point, k is the electron wave-vector component along ζ, and κ is along $\mathbf{C}_h$ (see Fig. 1). It is convenient to perform a unitary transformation to remove the dependence on the chirality angle θ from the Hamiltonian, i.e.,

$$U=\begin{pmatrix} e^{i\tau_3\theta} & 0 \\ 0 & 1 \end{pmatrix}, \tag{2}$$

$$H_0=U\tilde{H}_0U^{-1}=\hbar v(\tau_3\kappa\sigma_1+k\sigma_2). \tag{3}$$

Eigenvalues and eigenfunctions [in the rotated reference frame (φ,ζ)] of the Hamiltonian (3) at zero magnetic field are given by

$$E_{\kappa,k}=\pm\hbar v\sqrt{\kappa^2+k^2}, \tag{4}$$

$$\Psi^{(\prime)}_{\kappa,k}(\varphi,\zeta)=\frac{e^{i\mathbf{K}^{(\prime)}\cdot\mathbf{r}}}{\sqrt{4\pi}}e^{i(\kappa R\varphi+k\zeta)}\begin{pmatrix} z^{(\prime)}_{\kappa_m,k} \\ 1 \end{pmatrix}, \tag{5}$$

$$z_{\kappa,k}=\pm\frac{(\kappa-ik)}{\sqrt{\kappa^2+k^2}},\quad z'_{\kappa,k}=\mp\frac{(\kappa+ik)}{\sqrt{\kappa^2+k^2}}, \tag{6}$$

where $\mathbf{r}=(R\varphi\cos\theta-\zeta\sin\theta, R\varphi\sin\theta+\zeta\cos\theta)$.

Periodic boundary conditions along the NT circumference [$\Psi(\mathbf{r}+C_h)=\Psi(\mathbf{r})$] quantize the wave vector associated with the $\mathbf{C}_h$ direction [$(\mathbf{k}+\mathbf{K}^{(\prime)})\cdot\mathbf{C}_h=2\pi m$, $m\in\mathbb{Z}$]: $\kappa\to(m-\tau_3\nu/3)/R$, where $m\in\mathbb{Z}$ and $\nu=0,\pm1$ are determined by $n_1-n_2=3N+\nu$ ($N\in\mathbb{Z}$).[4] A NT with $\nu=0$ [e.g., (n,n) armchair NT] has zero band gap and is called a metallic NT. Such a NT is not suitable to confine particles due to the Klein paradox in gapless structures.[21] Therefore, semiconducting NTs ($\nu=\pm1$) are more favorable for quantum dot realizations, and we focus on this case in the following. An additional feature of semiconducting NTs with $\nu=\pm1$ is that they allow us to avoid the problem of energy degeneracy at the $\mathbf{K}$ and $\mathbf{K}'$ points by applying an Aharonov–Bohm flux $\Phi_{AB}=B\pi R^2$ through the NT cross section.[4] Lifting the degeneracy is crucial for spin qubit realizations with controlled interqubit exchange.[22] The Aharonov–Bohm flux leads to a shift of the quantum number $m\to m+\Phi_{AB}/\Phi_0$ ($\Phi_0=hc/|e|$ is the flux quantum) and to a Zeeman splitting $E_{\kappa_m,k}\to E_{\kappa_m,k,S_\zeta}=E_{\kappa_m,k}+S_\zeta\hbar\omega_Z$, where $\omega_Z=|e|gB/2m_0c$, $S_\zeta=\pm1/2$ is the spin projection on the NT axis. Therefore, the energy spectrum and wave function of an electron in a NT are given by

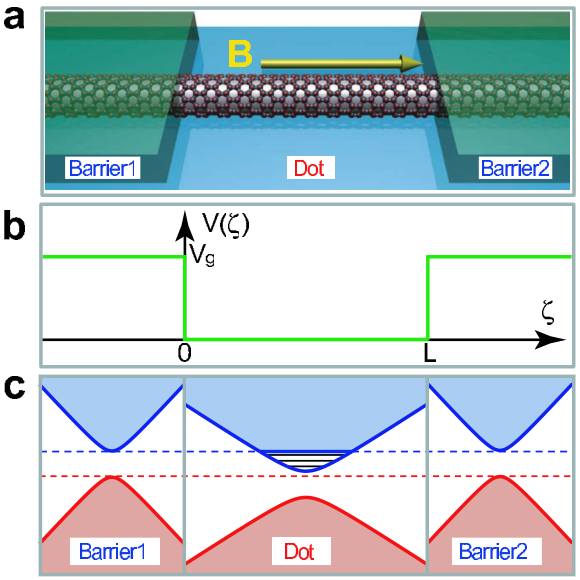

FIG. 2. (Color online) Nanotube quantum dot. (a) Nanotube with two top gates. (b) Longitudinal confinement potential. (c) Scheme of the band structure.

$$E_{\kappa_m,k,S_\zeta}=E_{\kappa_m,k}+S_\zeta\hbar\omega_Z, \tag{7}$$

$$\Psi^{(\prime)}_{\kappa_m,k,S_\zeta}(\varphi,\zeta)=\Psi^{(\prime)}_{\kappa_m,k}(\varphi,\zeta)|S_\zeta\rangle, \tag{8}$$

where $\kappa_m=(m+\Phi_{AB}/\Phi_0-\tau_3\nu/3)/R$, and $|S_\zeta\rangle$ is the spin part of the wave function.

Now we consider a quantum dot (QD) which is made of a NT by the deposition of top gates on the NT (Refs. 16–18) [see Fig. 2(a)]. The spacing between the gates L defines the length of a QD. We describe the confinement by the rectangular potential [see Fig. 2(b)],

$$V(\zeta)=\begin{cases} V_g, & \zeta<0 \text{ or } \zeta>L, \\ 0, & 0\le\zeta\le L. \end{cases} \tag{9}$$

Recent experimental realizations of a NT QD[23–25] provide clear evidence favoring the rectangular confinement in a QD, since Fabry–Pérot interference observed in such experiments is a testimony for a NT QD with a well-defined length. Note that we consider the experimentally more accessible case, when the length of a NT QD L is much larger than its radius R ($L\approx100$ nm). For such QDs, the steplike potential drop happens on a length scale much larger than the lattice con-

stant. Therefore, it does not introduce intervalley scattering.

Straightforward calculations show that the bottom of the mth subband of the NT spectrum *under* the top gates $\hbar v|\kappa_m|+V_g$ divides the spectrum *between the gates* for this subband into two parts. Above the energy $\hbar v|\kappa_m|+V_g$ [dashed blue line in Fig. 2(c)], the spectrum is continuous $E_{\kappa_m,k}$ $(|k|\geq(|V_g|/\hbar v)\sqrt{1+2\hbar v|\kappa_m|/V_g})$ and below there is a discrete spectrum E_{κ_m,k_n},

$$E_{\kappa_m,k,S_\zeta}=\begin{cases}E_{\kappa_m,k_n,S_\zeta} & (k=k_n\leq k_c),\\ E_{\kappa_m,k,S_\zeta} & (|k|>k_c,k\in\mathbb{R}),\end{cases} \tag{10}$$

where $k_c=(|V_g|/\hbar v)\sqrt{1+2\hbar v|\kappa_m|/V_g}$ and allowed values of the quantized wave vector k_n along the NT axis are found from the transcendental equation,

$$\tan k_nL=\frac{(\hbar v)^2\tilde{k}_nk_n}{E_{\kappa_m,k_n}(E_{\kappa_m,k_n}-V_g)-(\hbar v)^2\kappa_m^2}. \tag{11}$$

Here, $\tilde{k}_n=\sqrt{\kappa_m^2-(E_{\kappa_m,k_n}-V_g)^2/(\hbar v)^2}$. The wave function of an electron in a NT QD can be written as follows:

$$\Psi^{(\prime)}_{\kappa_m,k,S_\zeta}(\varphi,\zeta)=\frac{e^{i\mathbf{K}^{(\prime)}\cdot\mathbf{r}}}{\sqrt{2\pi}}e^{i(m-\tau_3\nu/3+\Phi_{AB}/\Phi_0)\varphi}\Phi_{m,k}(\zeta)|S_\zeta\rangle, \tag{12}$$

where

$$\Phi_{m,k}(\zeta)=\begin{cases}\Phi^L_{m,k}(\zeta), & \zeta<0,\\ \Phi^D_{m,k}(\zeta), & 0\leq\zeta\leq L,\\ \Phi^R_{m,k}(\zeta), & \zeta>L.\end{cases} \tag{13}$$

Here, for a discrete spectrum $(k=k_n\leq k_c)$,

$$\Phi^L_{m,k_n}(\zeta)=Ae^{\tilde{k}_n\zeta}\begin{pmatrix}z^{(\prime)}_{\kappa_m,-i\tilde{k}_n}\\1\end{pmatrix}, \tag{14}$$

$$\Phi^D_{m,k_n}(\zeta)=\left[Ce^{ik_n\zeta}\begin{pmatrix}z^{(\prime)}_{\kappa_m,k_n}\\1\end{pmatrix}+De^{-ik_n\zeta}\begin{pmatrix}z^{(\prime)}_{\kappa_m,-k_n}\\1\end{pmatrix}\right], \tag{15}$$

$$\Phi^R_{m,k_n}(\zeta)=Be^{\tilde{k}_n(L-\zeta)}\begin{pmatrix}z^{(\prime)}_{\kappa_m,i\tilde{k}_n}\\1\end{pmatrix}, \tag{16}$$

where

$$C=A\frac{z^{(\prime)}_{\kappa_m,-k_n}-z^{(\prime)}_{\kappa_m,-i\tilde{k}_n}}{z^{(\prime)}_{\kappa_m,-k_n}-z^{(\prime)}_{\kappa_m,k_n}},\quad D=A\frac{z^{(\prime)}_{\kappa_m,-i\tilde{k}_n}-z^{(\prime)}_{\kappa_m,k_n}}{z^{(\prime)}_{\kappa_m,-k_n}-z^{(\prime)}_{\kappa_m,k_n}}, \tag{17}$$

$$B=A\left\{e^{ik_nL}\frac{z^{(\prime)}_{\kappa_m,-k_n}-z^{(\prime)}_{\kappa_m,-i\tilde{k}_n}}{z^{(\prime)}_{\kappa_m,-k_n}-z^{(\prime)}_{\kappa_m,k_n}}+e^{-ik_nL}\frac{z^{(\prime)}_{\kappa_m,-i\tilde{k}_n}-z^{(\prime)}_{\kappa_m,k_n}}{z^{(\prime)}_{\kappa_m,-k_n}-z^{(\prime)}_{\kappa_m,k_n}}\right\}, \tag{18}$$

and A can be found from the normalization condition,

$$1=\|\Psi\|^2=|A|^2[(z^{(\prime)}_{\kappa_m,-i\tilde{k}_n})^2+1]\frac{1}{2\tilde{k}_n}+|B|^2[(z^{(\prime)}_{\kappa_m,i\tilde{k}_n})^2+1]\frac{1}{2\tilde{k}_n}+4L|C|^2+\mathrm{Re}\left[C^*D[(z^{(\prime)}_{\kappa_m,-k_n})^2+1]\frac{1}{ik_n}(1-e^{-2ik_nL})\right]. \tag{19}$$

For the **K** point, we obtain

$$C=A\frac{1}{2}+i\ \mathrm{Im}\ C,\quad D=A\frac{1}{2}-i\ \mathrm{Im}\ C, \tag{20}$$

$$\mathrm{Im}\ C=\frac{A\kappa_m}{2k_n}\left(-1+\frac{E_{\kappa_m,k_n}}{E_{\kappa_m,k_n}-V_g}\frac{\kappa_m-\tilde{k}_n}{\kappa_m}\right)=-\frac{AE_{\kappa_m,k_n}}{2k_n}\left(\frac{\kappa_m}{E_{\kappa_m,k_n}}-\frac{\kappa_m-\tilde{k}_n}{E_{\kappa_m,k_n}-V_g}\right), \tag{21}$$

$$B=A\cos(k_nL)\frac{\kappa_m}{\kappa_m+\tilde{k}_n}\left[1+\frac{\tilde{k}_n^2}{E_{\kappa_m,k_n}(E_{\kappa_m,k_n}-V_g)-(\hbar v\kappa_m)^2}\right]. \tag{22}$$

For a continuous spectrum $(|k|>k_c)$, we make the following ansatz:

$$\Phi^L_{m,k}(\zeta)=e^{i\tilde{k}\zeta}\begin{pmatrix}z_{\kappa_m,\tilde{k}}\\1\end{pmatrix}+Re^{-i\tilde{k}\zeta}\begin{pmatrix}z_{\kappa_m,-\tilde{k}}\\1\end{pmatrix}, \tag{23}$$

$$\Phi^D_{m,k}(\zeta)=A_ce^{ik\zeta}\begin{pmatrix}z_{\kappa_m,k}\\1\end{pmatrix}+B_ce^{-ik\zeta}\begin{pmatrix}z_{\kappa_m,-k}\\1\end{pmatrix}, \tag{24}$$

$$\Phi^R_{m,k}(\zeta)=Te^{i\tilde{k}(\zeta-L)}\begin{pmatrix}z_{\kappa_m,\tilde{k}}\\1\end{pmatrix}, \tag{25}$$

where

$$|k|\geq(|V_g|/\hbar v)\sqrt{1+2\hbar v|\kappa_m|/V_g},$$

$$\tilde{k}=\pm\sqrt{[(E_{\kappa_m,k}-V_g)/\hbar v]^2-(\kappa_m)^2},$$

and find that

$$A_c=e^{-ikL}\frac{(z_{\kappa_m,-k}-z_{\kappa_m,\tilde{k}})(z_{\kappa_m,\tilde{k}}-z_{\kappa_m,-\tilde{k}})\sqrt{\kappa_m^2+\tilde{k}^2}\sqrt{\kappa_m^2+k^2}}{4[\tilde{k}k\cos(kL)-i\sin(kL)(\sqrt{\kappa_m^2+\tilde{k}^2}\sqrt{\kappa_m^2+k^2}-\kappa_m^2)]}, \tag{26}$$

$$B_c=\frac{z_{\kappa_m,\tilde{k}}-z_{\kappa_m,-\tilde{k}}}{z_{\kappa_m,-k}-z_{\kappa_m,-\tilde{k}}}-A_c\frac{z_{\kappa_m,k}-z_{\kappa_m,-\tilde{k}}}{z_{\kappa_m,-k}-z_{\kappa_m,-\tilde{k}}}, \tag{27}$$

$$R=A_c+B_c-1,\quad T=A_ce^{ikL}+B_ce^{-ikL}. \tag{28}$$

III. SPIN-ORBIT INTERACTION IN NANOTUBES

Next, we take SOI effects into account. In graphene, there are two main mechanisms of SOI: Intrinsic SOI, H_{SO}^{int}

$=\Delta_{\text{int}}\tau_3\sigma_3 s_z$,[26] and extrinsic SOI (Bychkov–Rashba type), $H_{\text{SO}}^{\text{ext}}=(\Delta_E+\Delta_{\text{curv}})(\tau_3\sigma_1 s_y-\sigma_2 s_x)$, which is due to the asymmetric confinement potential normal to the graphene sheet (Δ_E) [26] and curvature induced effective electric field of rippled graphene (Δ_{curv}) [27] (where s_j is the Pauli spin matrix). In a NT, i.e., a graphene sheet rolled up into a cylinder, the spin components perpendicular to the NT axis become dependent on the polar angle φ,[28]

$$s_x = i(-S_+e^{i\varphi}+S_-e^{-i\varphi}), \tag{29}$$

$$s_y = 2S_\zeta, \tag{30}$$

$$s_z = S_+e^{i\varphi}+S_-e^{-i\varphi}, \tag{31}$$

where, in the eigenbasis of S_ζ, $2S_\zeta|\uparrow\rangle=|\uparrow\rangle$, $2S_\zeta|\downarrow\rangle=-|\downarrow\rangle$, $S_+|\uparrow\rangle=S_-|\downarrow\rangle=0$, $S_+|\downarrow\rangle=|\uparrow\rangle$, and $S_-|\uparrow\rangle=|\downarrow\rangle$. Therefore, for a NT, the intrinsic SOI Hamiltonian is given by

$$H_{\text{SO}}^{\text{int}} = \Delta_{\text{int}}\tau_3\sigma_3(S_+e^{i\varphi}+S_-e^{-i\varphi}), \tag{32}$$

the extrinsic SOI term due to Δ_E is given by

$$H_{\text{SO}}^{E} = \Delta_E[2\tau_3\sigma_1 S_\zeta - i\sigma_2(-S_+e^{i\varphi}+S_-e^{-i\varphi})], \tag{33}$$

and the extrinsic SOI term due to curvature of a NT is given by[28]

$$H_{\text{SO}}^{\text{curv}} = i\Delta_{\text{curv}}^{\perp}\sigma_2(-S_+e^{i\varphi}+S_-e^{-i\varphi})+\Delta_{\text{curv}}^{\parallel}\tau_3\sigma_1 2S_\zeta, \tag{34}$$

where $\Delta_{\text{curv}}^{\perp}=-\Delta(V_{pp}^{\sigma}-V_{pp}^{\pi})a_0/8\sqrt{3}R\varepsilon_{\pi\sigma}$ and $\Delta_{\text{curv}}^{\parallel}=\Delta(3V_{pp}^{\sigma}+5V_{pp}^{\pi})a_0/8\sqrt{3}R\varepsilon_{\pi\sigma}$ [$\Delta=12$ meV,[29] $\varepsilon_{\pi\sigma}=7.3$ eV, $V_{pp}^{\sigma}=6.38$ eV, and $V_{pp}^{\pi}=-2.66$ eV (Ref. 30)]. Note that at moderate electric fields ($E<0.1$ V/nm), the last SOI term is dominant [$\Delta_{\text{int}}\approx 1$ μeV,[27] $\Delta_E<\Delta_{\text{int}}$, and $\Delta_{\text{curv}}^{\perp}\approx-(0.26\ \text{meV}/R[\text{nm}])$] and, therefore, the other types of SOI can be safely neglected.

The last term $\propto\Delta_{\text{curv}}^{\parallel}S_\zeta$ [where $\Delta_{\text{curv}}^{\parallel}\approx 0.17\ \text{meV}/R[\text{nm}]$] in Eq. (34) leads to a shift $\kappa_m\to\varkappa_m^{\pm}=\kappa_m\pm\Delta_{\text{curv}}^{\parallel}/\hbar v$ (Ref. 28) (where $\pm$ corresponds here to $|\uparrow\rangle$ and $|\downarrow\rangle$ states) and, therefore, to a spin splitting,

$$E_{\varkappa_m^+,k_n,+1/2}-E_{\varkappa_m^-,k_n,-1/2}\approx\hbar\omega_Z-2\ \text{sgn}(m-\tau_3\nu/3)\Delta_{\text{curv}}^{\parallel} \tag{35}$$

(for $|\varkappa_m^{\pm}|\gg k_n$). Thus, SOI $\propto\Delta_{\text{curv}}^{\parallel}$ acts as an effective magnetic field resulting in a level splitting ($2\Delta_{\text{curv}}^{\parallel}$) at zero magnetic field, as has been experimentally confirmed now.[31] Note that this zero-field splitting does not violate Kramers theorem since time reversed states correspond to different nonequivalent **K** points and are degenerate at zero B fields (see Fig. 3). The existence of the zero-field splitting opens up an intriguing possibility for spin resonance experiments *without* any magnetic fields: the first term in Eq. (34) allows electric-dipole transitions between spin-up and spin-down states, the second term (as an effective magnetic field) splits these states, and thus oscillating electric fields perpendicular to a NT lead to electric-dipole spin resonance with resonance frequency $\omega=2\Delta_{\text{curv}}^{\parallel}/\hbar\approx 33\times10^{10}$ s^{-1} and Rabi frequency $\omega_{\text{R}}\approx 1.6\times10^5$ s^{-1} at $E=10$ V/cm and $V_g=2.3$ meV (see Appendix A).

We know that intervalley mixing leads to splitting of the levels corresponding to different **K** points, which has been observed in Ref. 32. Such mixing does not split Kramers doublets (in the case of time reversal symmetric intervalley scattering) but modifies the magnitude of the splitting ($2\Delta_{\text{curv}}^{\parallel}\to 2\sqrt{\Delta_{\text{curv}}^{\parallel 2}+\Delta_{\mathbf{K}-\mathbf{K}'}^2}$, where $\Delta_{\mathbf{K}-\mathbf{K}'}$ is the intervalley mixing strength) between spin-up and spin-down states of a certain **K** point and leads to anticrossings at nonzero B fields of the levels with the same spin orientation but belonging to different **K** valleys (see Fig. 3 and Appendix B).

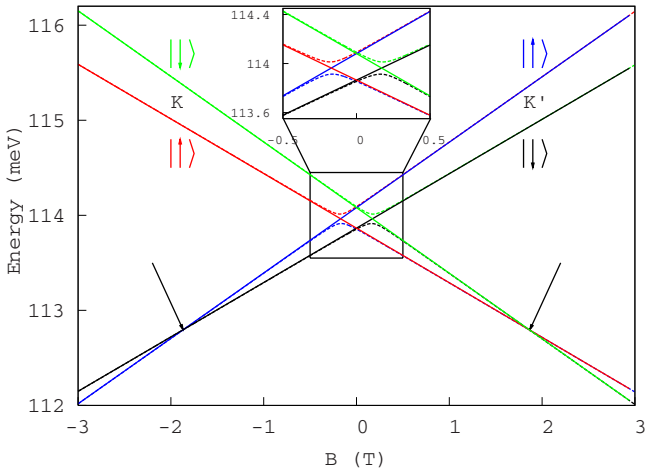

FIG. 3. (Color online) Lowest energy levels of electrons in a NT QD at low magnetic fields ($R\approx 1.6$ nm, $L=100$ nm, $g=2$, and $V_g=\hbar v/40R\approx 8.5$ meV). The solid curves correspond to the case of zero intervalley mixing. At zero magnetic fields there is splitting of the levels due to the second term in Eq. (34). The magnitude of the splitting is $2\Delta_{\text{curv}}^{\parallel}=0.22$ meV. The arrows indicate crossings of $|\uparrow\rangle$ and $|\downarrow\rangle$ states of a certain **K** point. At these level crossings, a singularity appears in $1/T_1$ (see below in Fig. 6). The dashed curves correspond to the case of weak intervalley mixing ($\Delta_{\mathbf{K}-\mathbf{K}'}=0.05$ meV). It modifies the zero-field splitting $2|\Delta_{\text{curv}}^{\parallel}|\to 2\sqrt{\Delta_{\text{curv}}^{\parallel 2}+\Delta_{\mathbf{K}-\mathbf{K}'}^2}$ and opens up avoided crossings (with the value $2|\Delta_{\mathbf{K}-\mathbf{K}'}|$) of the levels with the same spin orientation but different valley index. This is illustrated in the inset which is a blow-up of the center region of the spectrum.

In the case of negative voltage applied to the top gates ($V_g<0$), hole states become localized instead of electrons. It can be shown that the energy spectrum of the lowest levels of holes has the same structure as for electrons (illustrated in Fig. 3) but shifted down by the energy gap $E_g\approx 2\hbar v\sqrt{\kappa_0^2+k_0^2}\approx 228$ meV. From Fig. 3, we see that electron energy levels cross at $\hbar\omega_Z=2\tau_3\nu\Delta_{\text{curv}}^{\parallel}$ (indicated by arrows in Fig. 3), whereas there are no crossings of the two highest levels of holes at nonzero magnetic fields. Therefore, SOI (due to zero-field splitting of energy levels) breaks the electron-hole symmetry. For the estimation of the SOI constants, we use band parameters of bulk graphite. Note that for small radius NT, due to curvature effects, strong hybridization of bands can modify the band parameters of a NT and, thus, the SOI constants or the g factor. If the SOI constant had the opposite sign due to hybridization, then the energy spectrum for electrons would look like the one for holes and vice versa.[31] Hence, in the case of negative $\Delta_{\text{curv}}^{\parallel}$, there are crossings of levels for holes and not for electrons (at $B\neq 0$). Such electron-hole asymmetry in the spectrum can provide

us with information about the sign and the magnitude of the SOI constant and about the g factor.

Now, we turn to the quantitative discussion of the spin relaxation time in nanotube quantum dots. We take the first term in Eq. (34) into account in the framework of perturbation theory, which leads to the solution of the Dirac (eigenvalue) equation for the lowest levels $(H_0 \pm \hbar\omega_Z/2 + H_{\mathrm{SO}}^{\mathrm{curv}})\psi_{0,0,\pm 1/2} = \mathcal{E}_{0,0,\pm 1/2}\psi_{0,0,\pm 1/2}$ in first order in $H_{\mathrm{SO}}^{\mathrm{curv}}$,

$$\mathcal{E}_{0,0,\pm 1/2} \approx E_{\varkappa_0^{\pm},k_0,\pm 1/2}, \tag{36}$$

$$\psi_{0,0,\pm 1/2}(\varphi,\zeta) \approx \Psi_{\varkappa_0^{\pm},k_0,\pm 1/2}(\varphi,\zeta) + \sum_{n\neq 0} \lambda_{k_n}^{\mp}\Psi_{\varkappa_{\mp 1}^{\mp},k_n,\mp 1/2}(\varphi,\zeta) + \frac{L}{2\pi}\int_{\pm k_c}^{\pm\infty} dk\lambda_k^{\mp}\Psi_{\varkappa_{\mp 1}^{\mp},k,\mp 1/2}(\varphi,\zeta), \tag{37}$$

$$\lambda_k^{\pm} = \pm i\Delta_{\mathrm{curv}}^{\perp}\frac{\langle\Phi_{\varkappa_{\pm 1}^{\pm},k}(\zeta)|\sigma_2|\Phi_{\varkappa_0^{\mp},k_0}(\zeta)\rangle}{E_{\varkappa_{\pm 1}^{\pm},k,\pm 1/2} - E_{\varkappa_0^{\mp},k_0,\mp 1/2}}. \tag{38}$$

Note that the function $[\Phi_{\varkappa_{m'}^{\pm},k_{n'}}(\zeta)]^{\dagger}\sigma_2\Phi_{\varkappa_m^{\mp},k_n}(\zeta)$ is either symmetric or antisymmetric with respect to inversion at $\zeta = L/2$. Hence, there is a selection rule for SOI between quantized levels, namely,

$$\langle\Phi_{\varkappa_{m'}^{\pm},k_{n'}}(\zeta)|\sigma_2|\Phi_{\varkappa_m^{\mp},k_n}(\zeta)\rangle \propto 1 - \mathrm{sgn}(m' - 1/3)\mathrm{sgn}(m - 1/3)(-1)^{n'+n}. \tag{39}$$

Thus, $\lambda_{k_{n'}}^{+}=0$ $(\lambda_{k_{n'}}^{-}=0)$ for odd (even) n'.

IV. ELECTRON-PHONON COUPLING IN NANOTUBES

For definiteness, we consider only such (n_1,n_2) NTs that $n_1-n_2=3N+1$ $(\nu=1)$. Then the two states $(\psi_{0,0,\pm 1/2})$ with the lowest energy (at $\Phi_{\mathrm{AB}}/\Phi_0 > \Delta_{\mathrm{curv}}^{\parallel}R/\hbar v$) of a NT QD belong to the **K** point with $\tau_3=1$ (see Fig. 3). Phonon induced transitions (which become allowed due to SOI) between these states give the dominant contribution to spin relaxation of a single particle in a NT QD. Despite quite complicated phonon dispersion relations in NTs,[33] it is possible to find analytical expressions for the electron-phonon coupling in NTs in the case of low-energy phonons.

The splitting between the $\mathcal{E}_{0,0,\pm 1/2}$ states is less than 1 meV at $B<10$ T. Phonons with much higher energies are not favorable for transitions between these levels. The energy of the radial breathing mode is $\hbar\omega_{\mathrm{RBM}} > 8.5$ meV (Ref. 34) for NTs with $R \leq 1.5$ nm, which excludes that mode (and all higher modes) from our analysis. Thus, only three acoustic phonon modes are important for spin-flip transitions between the lowest two levels: the twisting mode (TM), the stretching mode (SM), and the bending mode (BM).[4] To describe these modes we use a continuum model,[4] in which the equation of motion for the displacement $\mathbf{u}(\mathbf{r},t)=(u_\varphi,u_\zeta,u_r)$ is given by

$$\ddot{\mathbf{u}}(\mathbf{r},t) = \Lambda\mathbf{u}(\mathbf{r},t), \tag{40}$$

where the force-constant tensor

$$\Lambda = \begin{pmatrix} \frac{c_l^2}{R^2}\nabla_{\varphi\varphi}^2 + c_t^2\nabla_{\zeta\zeta}^2 & \frac{c_l^2-c_t^2}{R}\nabla_{\varphi\zeta}^2 & \frac{c_l^2}{R}\nabla_r \\ \frac{c_l^2-c_t^2}{R}\nabla_{\varphi\zeta}^2 & c_l^2\nabla_{\zeta\zeta}^2 + \frac{c_t^2}{R^2}\nabla_{\varphi\varphi}^2 & \frac{c_l^2-2c_t^2}{R}\nabla_r \\ -\frac{c_l^2}{R}\nabla_r & -\frac{c_l^2-2c_t^2}{R}\nabla_\zeta & -\frac{c_l^2}{R^2} \end{pmatrix} \tag{41}$$

is invariant under the group symmetry operations of a NT.[4,35] Here, c_l and c_t are the longitudinal and transverse phonon velocities, respectively [$c_l=20.9$ km/s and $c_t=12.3$ km/s (Ref. 36)]. Substituting the solution of Eq. (40) in the form $\mathbf{u}(\mathbf{r},t)=\mathbf{A}_\alpha\exp[i(m\varphi+q\zeta-\omega t)]$ (where q and ω are the phonon wave vector and frequency, respectively, and α is the phonon mode) and keeping only leading terms in qR $(qR \ll 1)$, we get for TM phonons $(m=0)$,

$$\omega_T = c_t q, \quad \mathbf{A}_T = A_T(1,0,0), \tag{42}$$

for SM phonons $(m=0)$,

$$\omega_S = c_S q, \quad \mathbf{A}_S = A_S(0,1,-iqR\eta), \tag{43}$$

and for BM phonons $(m=1)$,

$$\omega_B = c_S R q^2/\sqrt{2}, \tag{44}$$

$$\mathbf{A}_B = \frac{A_B}{\sqrt{2}}\left(i + \frac{i\eta(qR)^2}{2}, -iqR, 1 - \frac{\eta(qR)^2}{2}\right), \tag{45}$$

where $c_S = 2(c_t/c_l)\sqrt{c_l^2-c_t^2}$, $\eta=(c_l^2-2c_t^2)/c_l^2$, and $A_j=\sqrt{\hbar/2M\omega_j}$ (where M is the NT mass). We see that TM and SM show linear dispersion, whereas BM exhibits quadratic dispersion. Note that these results are only valid for long-wavelength phonons ($qR \ll 1$ and $\omega < \omega_{\mathrm{RBM}}$).

The electron-phonon coupling is expressed by the operator

$$V_{\text{el-ph}} = \begin{pmatrix} V_1 & V_2 \\ V_2^* & V_1 \end{pmatrix} + \text{H.c.}, \tag{46}$$

where for the **K** point,

$$V_1 = g_1(u_{\varphi\varphi} + u_{\zeta\zeta}), \quad V_2 = g_2 e^{3i\theta}(u_{\varphi\varphi} - u_{\zeta\zeta} + 2iu_{\varphi\zeta}), \tag{47}$$

$$u_{\varphi\varphi} = \frac{1}{R}\frac{\partial u_\varphi}{\partial\varphi} + \frac{u_r}{R}, \quad u_{\zeta\zeta} = \frac{\partial u_\zeta}{\partial\zeta}, \quad 2u_{\varphi\zeta} = \frac{\partial u_\varphi}{\partial\zeta} + \frac{1}{R}\frac{\partial u_\zeta}{\partial\varphi}, \tag{48}$$

$g_1 \approx 30$ eV is the deformation potential constant (which appears in diagonal elements of $V_{\text{el-ph}}$), and the off-diagonal coupling constant $g_2 \approx 1.5$ eV (which is caused by change in the bond-length between neighboring carbon atoms).[36] Using Eqs. (42)–(46), we get for the TM

$$V_1^T = 0, \quad V_2^T = -g_2 A_T q e^{3i\theta} e^{i(q\zeta-\omega_T t)}, \tag{49}$$

for the SM,

$$V_1^S = 2ig_1 A_S q \frac{c_t^2}{c_l^2} e^{i(q\zeta-\omega_S t)}, \quad V_2^S = ig_2 A_S q \frac{c_S^2}{c_t^2} e^{3i\theta} e^{i(q\zeta-\omega_S t)}, \tag{50}$$

and for the BM,

$$V_1^B = \sqrt{2} g_1 A_B q^2 R \frac{c_t^2}{c_l^2} e^{i(\varphi+q\zeta-\omega_B t)},$$

$$V_2^B = g_2 A_B q^2 R \frac{c_S^2}{\sqrt{2}c_t^2} e^{3i\theta} e^{i(\varphi+q\zeta-\omega_B t)}. \tag{51}$$

Note that the electron-phonon coupling in nanotubes is very strong (for example, compare $g_1 \approx 30$ eV with a deformational acoustic coupling constant in GaAs $\Xi_0 \approx 6.5$ eV). Furthermore, the electron wave function is highly localized in the dot region (it decays exponentially outside the dot). Thus, the phonons in the contacts or substrate can be safely ignored for our purposes. Moreover, we neglect the effect of the substrate on the phonon modes. This is justified due to the relatively weak coupling between the substrate and the NT, very high stiffness and rigidity of a NT, and, last but not least, very small atomic displacement amplitudes in an acoustic phonon wave (which is a few percents of Angstroms only).

V. SPIN RELAXATION IN NANOTUBES

We are now able to analyze spin-flip transitions between the lowest energy levels induced by long-wavelength phonons. Using Eq. (37), the matrix element of such a transition is given by

$$M_\omega \equiv \langle \psi_{0,0,-1/2} | V_{\text{el-ph}} | \psi_{0,0,1/2} \rangle = \sum_k \{ \lambda_k^- \langle \Psi_{\varkappa_0^-,k_0,-1/2} | V_{\text{el-ph}} | \Psi_{\varkappa_{-1}^-,k,-1/2} \rangle + (\lambda_k^+)^* \langle \Psi_{\varkappa_1^+,k,1/2} | V_{\text{el-ph}} | \Psi_{\varkappa_0^+,k_0,1/2} \rangle \}. \tag{52}$$

Here the sum stands for summation over the discrete k_n and integration over the continuous $|k| \geq (|V_g|/\hbar v)\sqrt{1+2\hbar v|\kappa_m|/V_g}$.

From Eq. (12), $\langle \Psi_{\kappa_{m_1},k_n,\pm 1/2} | e^{im_2\varphi} e^{iq\zeta} | \Psi_{\kappa_{m_3},k_{n'},\pm 1/2} \rangle = \langle \Phi_{m_1,k_n} | e^{iq\zeta} | \Phi_{m_3,k_{n'}} \rangle \delta_{m_1,m_2+m_3}$. Therefore, only phonon modes with $m_2=1$ give nonzero contribution to spin-flip transitions (this is an additional reason why we do not need to consider higher phonon modes with $m_2>1$). Thus, only BM phonons are responsible for the spin relaxation, whereas TM and SM phonons (with $m_2=0$) cannot flip the spin.

In the framework of Bloch–Redfield theory,[37] the spin relaxation time induced by BM phonons is given by

$$\frac{1}{T_1} = \frac{2\pi}{\hbar} L \int_{-\infty}^{\infty} dq (2N_\omega + 1) |M_\omega|^2 \delta\left(\hbar\omega_0 - \hbar \frac{c_S R}{\sqrt{2}q^2}\right) = \frac{2\pi}{\hbar} L \int_{-\infty}^{\infty} dq (2N_\omega + 1) |M_\omega|^2 \frac{1}{2^{3/4}\hbar\sqrt{c_S R \omega_0}} [\delta(q-q_0) + \delta(q+q_0)] = \frac{2^{5/4}\pi L}{\hbar^2 \sqrt{c_S R \omega_0}} (2N_{\omega_0}+1) |M_{\omega_0}|^2, \tag{53}$$

where $\omega_0 = |\mathcal{E}_{\varkappa_0^+,k_0,+1/2} - \mathcal{E}_{\varkappa_0^-,k_0,-1/2}|/\hbar \approx |\omega_Z - 2\tau_3 \Delta_{\text{curv}}^{\parallel}/\hbar|$, $q_0 = \sqrt{\sqrt{2}\omega_0/c_S R}$, and $N_\omega = [\exp(\hbar\omega/k_B T)-1]^{-1}$ is the Bose distribution function. Note that pure dephasing $1/T_\varphi = 0$ for BM phonons and $1/T_\varphi = O(\Delta_{\text{SO}}^4)$ for SM and TM phonons; therefore, $1/T_2 = 1/2T_1 + 1/T_\varphi = 1/2T_1$ in first-order perturbation theory.

We used the Markov and the secular approximations in the derivation of Eq. (53). We can estimate the correlation time in the phonon bath to be $\tau_c \approx 1$ ps. Therefore, the Markov approximation ($T_1 \gg \tau_c$) and the secular approximation ($\omega_0 T_1 \gg 1$) are valid except for the energy regime close to the level crossing at $\omega_0 = 0$. Moreover, our estimations of the electron-phonon coupling are valid for phonons with the wavelength shorter than the full length of the NT l_{NT}. Therefore, in the case of a small splitting between spin-up and spin-down states (long-wavelength phonons), the results are trustworthy for sufficiently long NTs ($l_{\text{NT}} q_0 \gg 1$), for example, if the spin splitting is 1 μeV, then the NT length should be greater than 700 nm.

We now study spin relaxation induced by low-frequency phonons ($\omega_0 \approx |\omega_Z - 2\tau_3 \Delta_{\text{curv}}^{\parallel}| \to 0$). As shown above, such spin relaxation occurs near the level crossing indicated by arrows in Fig. 3. One can show that $|M_{\omega_0}|^2 \propto \omega_0$ and $N_{\omega_0} \propto T/\omega_0$ (at $k_B T \gg \hbar\omega_0$) for $\omega_0 \to 0$. Moreover, the density of states for one-dimensional phonon modes with quadratic dispersion, i.e., the bending modes responsible for spin relaxation, has a van Hove singularity at zero frequency. It goes like $1/\sqrt{\omega_0}$, where ω_0 is the phonon frequency of the bending mode. This translates into the existence of a singularity in the noise spectral function $J(\omega_0) \propto 1/\sqrt{\omega_0}$, which describes particle spin relaxation due to coupling to NT lattice vibrations via SOI and electron-phonon interaction. Therefore,

$$1/T_1 \propto 1/\sqrt{\omega_0} \tag{54}$$

at low ω_0. To the best of our knowledge, this is the first system that exhibits a $1/\sqrt{\omega_0}$ spin-phonon noise spectrum at low frequencies. Such a result (fast relaxation times at small splitting between spin-up and spin-down levels) is counterintuitive in the light of the commonly expected long T_1 time for NTs (due to the expected weak SOI) and compared to the usual behavior of the spin relaxation time ($1/T_1 \propto \omega_Z^4$ at low magnetic fields) for conventional GaAs QDs.[9]

To better understand Eq. (54), we consider the spectral density of the electron-phonon correlation function,

$$J_{mk}(\omega) = \int_{-\infty}^{\infty} dt \overline{\langle m | V_{\text{el-ph}}(0) | k \rangle \langle k | V_{\text{el-ph}}(t) | m \rangle} e^{i\omega t},$$

where the overbar denotes the ensemble average. We first analyze this expression for GaAs QDs and later on for NT QDs.

For the phonon-induced relaxation rate between levels split by the Zeeman term, we find $1/T_1 \propto J_{12}(\omega_Z) \propto \Sigma_{\mathbf{q}} \Sigma_l (N_\omega + 1/2) |\langle 1 | A_\omega e^{i\mathbf{q}r} | l \rangle \langle l | H_{\text{SO}}^{\text{curv}} | 2 \rangle|^2 \delta(\omega - \omega_Z)$, where A_ω is the electron-phonon coupling strength and ω is the phonon frequency. Therefore, the correlation function defines the phonon-induced electron spin relaxation times. Let d be the single-phonon degree of freedom (related to the dimensionality of the underlying lattice structure). Then, for GaAs

semiconductor structures with linear in momentum H_{SO}^{curv}, we get $\Sigma_{\mathbf{q}} \to \int dq q^{d-1} \int d\Omega_{\mathbf{q}}$, $\langle 1|e^{i\mathbf{q}r}|l\rangle \propto q$ (in dipole approximation), $\langle l|H_{SO}^{curv}|2\rangle \propto \omega_Z$, and $N_\omega \propto 1/\omega$ (at $k_BT \gg \hbar\omega$). Taking into account that $A_\omega \propto 1/\sqrt{\omega}$ for the coupling between an electron and a piezoelectric phonon, we obtain $J_{12}(\omega_Z) \propto \omega_Z^{d+1}$ in the case of linear dispersion of a phonon ($\omega \propto q$). For deformational acoustic phonons, $A_\omega \propto \sqrt{\omega}$; therefore, $J_{12}(\omega_Z) \propto \omega_Z^{d+3}$. Therefore, at low frequency, the spectral density function of the electron-phonon coupling is super-Ohmic [$J(\omega) \propto \omega^n$, $n > 1$] even for all phonons in all dimensions.

This is fundamentally different for the NT QDs discussed here: Since H_{SO}^{curv} in a NT couples spin to the azimuthal degree of freedom [see Eq. (34)] and the azimuthal component of the phonon wave vector is quantized [see Eq. (51)], we get $\langle 1|A_\omega e^{i\mathbf{q}r}|l\rangle\langle l|H_{SO}^{curv}|2\rangle \propto 1 + O(q)$. Thus, for deformation-acoustic phonons ($A_\omega \propto \sqrt{\omega}$) with quadratic dispersion ($\Sigma_{\mathbf{q}} \to \int d\omega/\sqrt{\omega}$), we obtain $J_{12}(\omega_0) \propto 1/\sqrt{\omega_0}$ and recover Eq. (54). The noise spectral function $J_{12}(\omega)$ describes particle spin dissipation due to coupling to NT lattice vibrations (via SOI and electron-phonon interaction).

As shown in Fig. 6, the magnetic-field dependence of the spin relaxation rate of a NT QD is exceptional in comparison to that of a conventional semiconducting QD. First, there is a singularity of the electron spin relaxation rate at $\omega_0 \to 0$ (or at $\omega_Z \to 2\tau_3\Delta_{curv}^{\parallel}$) in contrast to the usual super-Ohmic behavior of $1/T_1$ in GaAs or InAs QDs (compare Fig. 6 with Fig. 1 in Ref. 9). Remarkably, the position of this symmetric singularity gives us a direct measurement of the SOI constant $\Delta_{curv}^{\parallel}$ and valley index τ_3 of an electron in a NT. The singularity is at positive magnetic fields for the **K** point ($\tau_3 = 1$) and at negative magnetic fields for the **K′** point ($\tau_3 = -1$). In Fig. 6, where $\tau_3 = 1$ and $2\Delta_{curv}^{\parallel} \approx 0.22$ meV, the singularity is at $B \approx 1.9$ T. If the SOI constants and g factors are the same for both electrons and holes, then the electron and hole spin relaxation curves map onto each other by a shift along the magnetic-field axis by $\Delta B = 2\Delta_{curv}^{\parallel}/g\mu_B$ (compare the blue and the red curves in Fig. 6).

We have also studied the chirality dependence of the spin relaxation rate as a function of the magnetic field. Different chirality nanotubes show qualitatively similar spin relaxation properties. In Fig. 4, the spin relaxation time for NT QDs with different chirality but approximately the same NT radius is shown. From this figure we conclude that T_1 depends on the chirality of a NT, although it has the same qualitative behavior as a function of a magnetic field.

VI. INTERFERENCE EFFECTS IN SPIN RELAXATION

We note here that the spin relaxation rate for flat GaAs QDs in in-plane magnetic fields is a monotonic function of B (up to about 14 T),[9] whereas, as shown in Fig. 6, it oscillates with B for NT QDs. The oscillations are caused by interference effects of two types: (i) interference of a *phonon wave* in a NT *electron* cavity bounded by the confining potential $V(\zeta)$ due to top gates (see Fig. 2) and (ii) interference between various contributions to the spin-flip transitions. For clarity, we will now study these two types of interference phenomena separately.

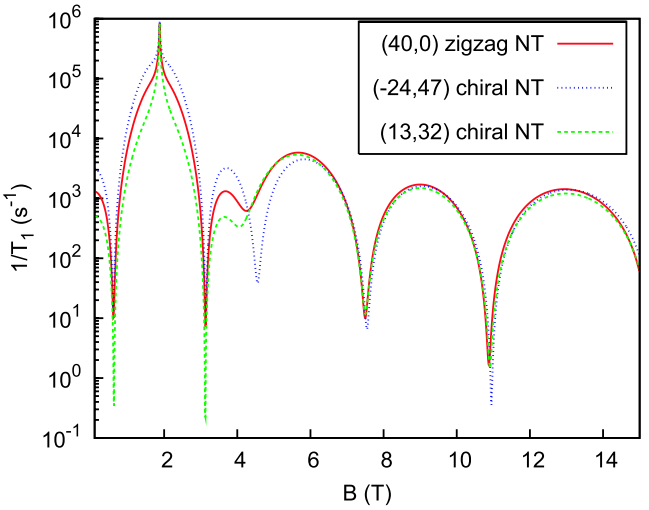

FIG. 4. (Color online) Chirality dependence of the electron spin relaxation for NT QDs. The spin relaxation rate as a function of a field for a (40,0) zigzag NT (solid curve, $\theta = 0$), (−24,47) NT (dotted curve, $\theta \approx \pi/2$), and (13,32) NT (dashed curve, $\theta \approx \pi/4$). $R \approx 1.6$ nm, $L = 100$ nm, $g = 2$, $V_g = \hbar v/40R \approx 8.5$ meV, and $T = 0.1$ K.

A. Interference of phonon waves

To illustrate the first effect, we only consider one contribution to spin-flip transitions, namely, that due to the first term in Eq. (52),

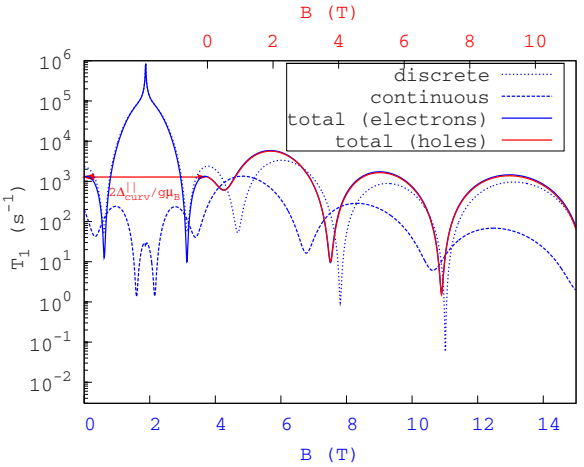

FIG. 5. (Color online) Spin relaxation of a (40,0) zigzag NT. The dependence of the electron and hole spin relaxation rates $1/T_1$ on a parallel magnetic field B (lower horizontal axis for electrons and upper one for holes) due to SO coupling of the two lowest states $(\Psi_{\varkappa_0^{\pm},k_0,\pm 1/2})$ to higher states of the discrete spectrum $(\Psi_{\varkappa_{\mp 1}^{\mp},k_n,\pm 1/2})$ is shown by the dashed curve and that due to SO coupling to states of the continuous spectrum $(\Psi_{\varkappa_{\mp 1}^{\mp},k,\mp 1/2})$ by the dotted curve. The total spin relaxation rate (solid curves) exhibits destructive interference at each odd crossing of the curves related to the abovementioned contributions [$R \approx 1.6$ nm, $L = 100$ nm, $g = 2$, $T = 0.1$ K, and $V_g = \pm\hbar v/40R \approx \pm 8.5$ meV, where the upper (lower) sign is for electrons (holes)]. The electron (blue solid curve) and the hole (red solid curve) spin relaxation time map onto each other by a shift along the magnetic-field axis by $\Delta B = 2\Delta_{curv}^{\parallel}/g\mu_B$.

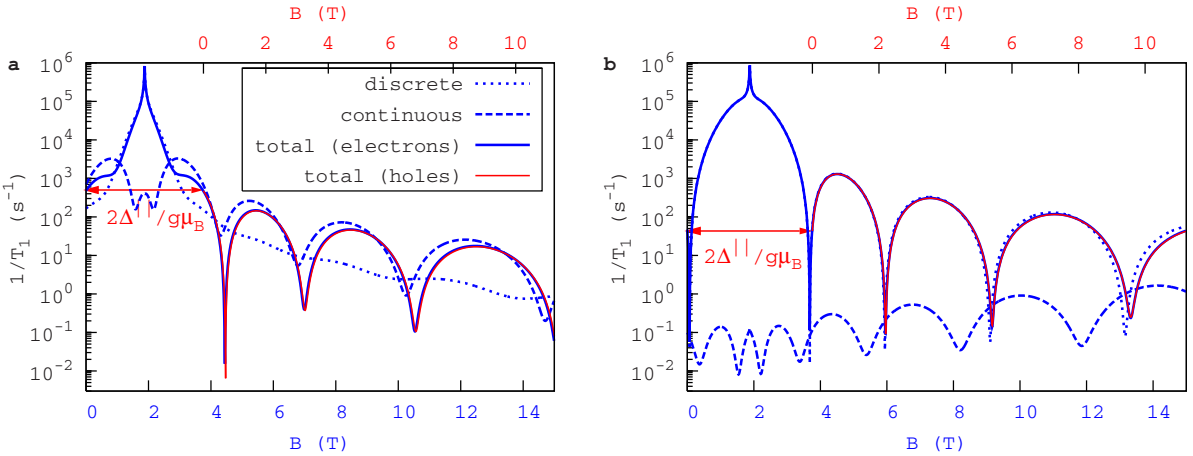

FIG. 6. (Color online) Spin relaxation of a (40,0) zigzag NT. The dependence of the electron and hole spin relaxation rates $1/T_1$ on a parallel magnetic field B (lower horizontal axis for electrons and upper one for holes) due to SOI of the two lowest states ($\Psi_{\varkappa_0^{\mp},k_0,\pm 1/2}$) to higher states of the discrete spectrum ($\Psi_{\varkappa_{\mp 1}^{\mp},k_n,\mp 1/2}$) is shown by the dashed curve and that due to SOI to states of the continuous spectrum ($\Psi_{\varkappa_{\mp 1}^{\mp},k,\mp 1/2}$) by the dotted curve. The total spin relaxation rate (solid curves) exhibits destructive interference at each odd crossing of the curves related to the abovementioned contributions [$R \approx 1.6$ nm, $L=100$ nm, $g=2$, $T=0.1$ K, (a) $V_g = \pm \hbar v/150R \approx \pm 2.3$ meV, and (b) $V_g = \pm \hbar v/3R \approx \pm 113$ meV, where the upper (lower) sign is for electrons (holes)]. The electron (blue solid curve) and the hole (red solid curve) spin relaxation time coincide by a shift along the magnetic-field axis by $\Delta B = 2\Delta^{\parallel}_{\mathrm{curv}}/g\mu_B$. In (a) (small V_g), the continuous spectrum substantially influences $1/T_1$. In contrast, in (b) (large V_g with many bound states in the dot), the discrete spectrum mainly determines the magnetic-field dependence of $1/T_1$.

$$M'_{\omega_0} = \lambda^{-}_{k_0} \langle \Psi_{\varkappa_0^{-},k_0,-1/2} | V_{\text{el-ph}} | \Psi_{\varkappa_{-1}^{-},k_0,-1/2} \rangle. \tag{55}$$

Note that $\lambda^{+}_{k_0}=0$ due to selection rules [see Eq. (39)]. The corresponding spin relaxation rate $1/T'_1$ due to this term only is shown in Fig. 7.

From Fig. 7, we see that $1/T'_1$ exhibits oscillations as a function of the ratio between the NT QD length L and the phonon wavelength λ_{ph}: $qL = 2\pi(L/\lambda_{\text{ph}})$. We attribute such oscillations to interferences of the phonon wave in a NT electron cavity bounded by the confining potential $V(\zeta)$ due to the top gates [see Eq. (9) and Fig. 2]. Such an interference effect is reminiscent of a Fabry–Pérot-type interference of a phonon wave where the electron levels in the dot play the role of a cavity. The coupling between the phonon wave and the cavity is described by the electron-phonon interaction $V_{\text{el-ph}}$.

At the minima in Fig. 7, the coupling between the electron cavity and the phonon waves becomes small. For an ideal cavity (with no loss), the matrix element of the spin-flip transition goes to zero at the minima. For instance, in the case of a rectangular hard wall potential, the squared modulus of the phonon-induced spin-flip transition is given by

$$\left| \left\langle \sqrt{\frac{2}{L}} \sin\frac{\pi x}{L} \middle| e^{iqx} \middle| \sqrt{\frac{2}{L}} \sin\frac{\pi x}{L} \right\rangle \right|^2 = \left(\frac{8\pi^2 \sin(qL/2)}{qL[4\pi^2 - (qL)^2]} \right)^2, \tag{56}$$

which is zero at $qL = 4\pi, 6\pi, 8\pi, \ldots$. Therefore, electron-phonon coupling is switched-off at these interference minima. In the case of a NT QD with a rectangular confining potential with finite barriers, however, due to the penetration of the electron wave function into classically forbidden region, the electron-phonon coupling is small but nonzero at the minima of the matrix element of the phonon-induced transition and the minima are shifted from those for an ideal cavity. As can be seen from Fig. 7, this shift and the minimal values of the electron-phonon coupling are more pronounced with increasing the barriers height V_g.

Interference effects in a NT QD occur only for confinement with well-defined length (for all bound states) and are absent for soft potentials such as parabolic confinement. Note, however, that the rectangular potential seems to be a good approximation for the confinement in a gated NT QD since Fabry–Pérot interferences (for electrons) have been observed in such a system.[23]

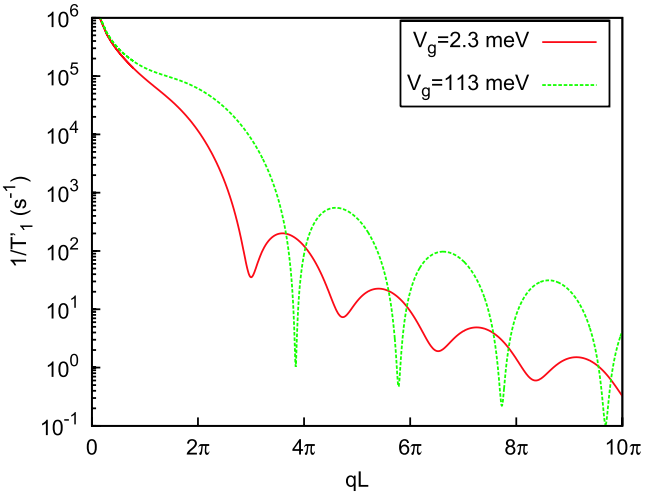

FIG. 7. (Color online) Interference phenomena in the spin relaxation rate due to the first contribution to the spin-flip transition ($\propto M'_{\omega_0}$). Here, q is the phonon wave vector and L is the length of the NT QD ($R \approx 1.6$ nm and $T=0.1$ K).

B. Coherence of different contributions to spin-flip process

In this section, we study interference effects due to various contributions to the spin-flip transitions described by Eq. (52). Let us consider the case of weak confinement with small $V_g=2.3$ meV. In this case, Eq. (52) can be rewritten as follows:

$$M_{\omega_B} = M_d^+ + M_d^- + M_c^+ + M_c^-,$$

$$M_d^+ = (\lambda_k^+)^* \langle \Psi_{\varkappa_1^+,k_0,1/2} | V_{\text{el-ph}} | \Psi_{\varkappa_0^+,k_0,1/2} \rangle$$

$$M_d^- = \lambda_k^- \langle \Psi_{\varkappa_0^-,k_0,-1/2} | V_{\text{el-ph}} | \Psi_{\varkappa_{-1}^-,k_1,-1/2} \rangle,$$

$$M_c^+ = \frac{1}{\pi} \int_{k_c^+}^{\infty} dk (\lambda_k^+)^* \langle \Psi_{\varkappa_1^+,k,1/2} | V_{\text{el-ph}} | \Psi_{\varkappa_0^+,k_0,1/2} \rangle,$$

$$M_c^- = \frac{1}{\pi} \int_{k_c^-}^{\infty} dk \lambda_k^- \langle \Psi_{\varkappa_0^-,k_0,-1/2} | V_{\text{el-ph}} | \Psi_{\varkappa_{-1}^-,k,-1/2} \rangle \quad (57)$$

($k_c^{\pm} = (|V_g|/\hbar v)\sqrt{1+2\hbar v|\varkappa_{\pm 1}^{\pm}|/V_g}$). Here M_d^+ and M_d^+ are contributions to the spin-flip transitions due to SOI of the two lowest levels ($\mathfrak{E}_{0,0,\pm 1/2}$) and higher *discrete* levels ($\mathfrak{E}_{1,0,+1/2}$ and $\mathfrak{E}_{-1,1,-1/2}$). Note that the coupling to other higher levels is forbidden by the selection rule Eq. (39). The contribution of these two terms to the spin relaxation rate is shown in Fig. 8. It can be seen that these two terms interfere (constructively), which leads to a change in the amplitude and period of the oscillations. Such constructive interference (see Fig. 8) between M_d^+ and M_d^- just increases the spin relaxation rate and, therefore, is not the dominant one. However, next we consider a different interference effect which reduces $1/T_1$ by several orders of magnitude.

1. Destructive interference

The remaining and most intriguing interference effect is the one between M_d^+ and M_c^+ (or between M_d^- and M_c^-). These terms are generated by SO coupling the two lowest states to the excited discrete and the continuous spectrum, respectively. From Figs. 5 and 6(a), we see that these contributions at some magnetic field interfere destructively leading to a strong increase of the spin relaxation time up to 4 orders of magnitude. Strikingly, such destructive interference is robust against a change of parameters, although being most evident when the terms $M_d^{\pm}$ and $M_c^{\pm}$ have comparable contributions to the spin-flip transitions [compare Figs. 6(a) and 6(b)].

Let us give a physical explanation for this phenomenon. First of all we note that the diagonal elements of the electron-phonon coupling ($\propto g_1$) [see Eq. (51) for details] give the main contribution to the spin-flip transitions with respect to the nondiagonal ones ($\propto g_2$) since $g_1 \gg g_2$. As a result, the destructive interference occurs due to diagonal elements of $V_{\text{el-ph}}$ and the elements $\propto g_2$ just modulate the strength of the effect, i.e., the depth of the dips in the spin relaxation curve. Therefore, in this section, we consider diagonal electron-phonon coupling ($\propto g_1$) only.

The terms of the spin-flip matrix element due to coupling to the first exited subband with $m=1$ [see Eq. (57)] can be written as follows:

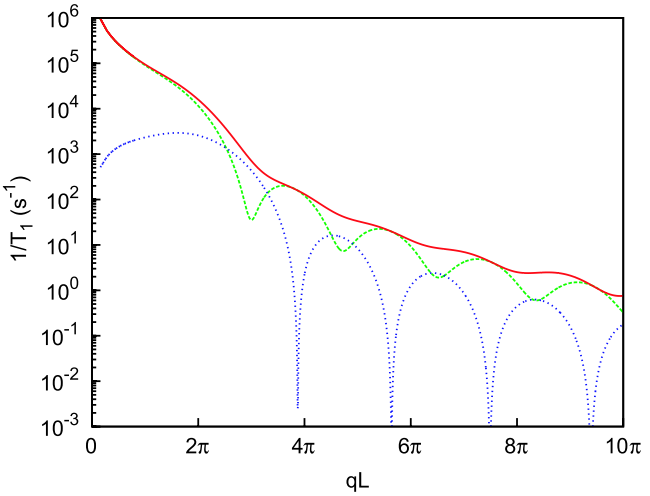

FIG. 8. (Color online) Spin relaxation rate due to M_d^+ (dashed curve) and M_d^- contribution (dotted curve) to spin-flip transition [see Eq. (57)]. The sum of these two contributions is plotted by solid curve ($R \approx 1.6$ nm, $g=2$, $T=0.1$ K, and $V_g = \hbar v/150R \approx 2.3$ meV).

$$M_d^+ = (\lambda_k^+)^* \langle \Psi_{\varkappa_1^+,k_0,1/2} | V_{\text{el-ph}} | \Psi_{\varkappa_0^+,k_0,1/2} \rangle \propto \int_{-\infty}^{\infty} d\zeta e^{iq_0\zeta} \Phi^{\dagger}_{\varkappa_1^+,k_0}(\zeta) \Phi_{\varkappa_0^+,k_0}(\zeta), \quad (58)$$

$$M_c^+ = \frac{1}{\pi} \int_{k_c^+}^{\infty} dk (\lambda_k^+)^* \langle \Psi_{\varkappa_1^+,k,1/2} | V_{\text{el-ph}} | \Psi_{\varkappa_0^+,k_0,1/2} \rangle \propto \int_{-\infty}^{\infty} d\zeta e^{iq_0\zeta} \int_{k_c^+}^{\infty} dk (\lambda_k^+)^* \Phi^{\dagger}_{\varkappa_1^+,k}(\zeta) \Phi_{\varkappa_0^+,k_0}(\zeta). \quad (59)$$

Note that $\Phi^{\dagger}_{\kappa_0^+,k_0}(\zeta)\Phi_{\kappa_0^+,k_0}(\zeta)$ is a symmetric function of ζ with respect to the center of the NT QD ($\zeta=L/2$). In the dot area ($0 \le \zeta \le L$), it might be approximated by a function $\propto \cos[\tilde{k}_0(L/2-\zeta)]$ with exponential tails in the classically forbidden areas ($\zeta<0$ and $\zeta>L$). In addition to the selection rule Eq. (39), it is easy to find that $\langle \Phi_{\kappa_{m'}^{\pm},k_{n'}}(\zeta) | \Phi_{\kappa_m^{\pm},k_n}(\zeta) \rangle = 1 + \text{sgn}(m'-1/3)\text{sgn}(m-1/3)(-1)^{n'+n}$ because $\Phi^{\dagger}_{\kappa_{m'}^{\pm},k_{n'}}(\zeta)$ $\Phi_{\kappa_m^{\pm},k_n}(\zeta)$ is either odd or even with respect to inversion at $\zeta=L/2$. Therefore, $M_d^+=0$ at $q_0=0$ since $\Phi^{\dagger}_{\varkappa_1^+,k_0}(\zeta)\Phi_{\varkappa_0^+,k_0}(\zeta)$ is an asymmetric function with respect to $\zeta=L/2$ at which it has a node. Thus, $\Phi^{\dagger}_{\varkappa_1^+,k_0}(\zeta)\Phi_{\varkappa_0^+,k_0}(\zeta)$ is found to be well approximated by a function $\sin(k'(L/2-\zeta))$ defined at $0 \le \zeta \le L$. Now we consider Eq. (59). After integration over k, we could assume that the dependence of $\Phi_{\varkappa_1^+,k}$ on ζ is integrated out; therefore, M_c^+ is a symmetric function of ζ with respect to $\zeta=L/2$, which we approximate by $-i\cos[k''(L/2-\zeta)]$ defined at $0 \le \zeta \le L$. Using these assumptions, we get the following estimations:

$$M_d^+ \propto \int_0^L d\zeta e^{iq_0\zeta} \sin[k'(L/2-\zeta)] = f_1(q_0L) + if_2(q_0L), \quad (60)$$

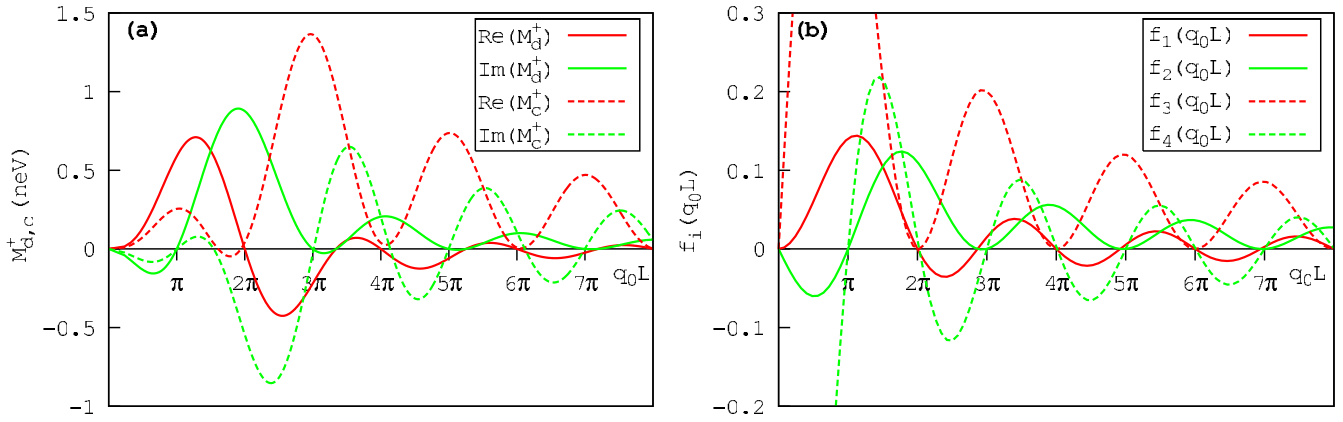

FIG. 9. (Color online) (a) Dependence of the real and imaginary parts of matrix elements M_d^+ and M_c^+ [see Eq. (57) for details] on the ratio of the NT length and phonon wavelength q_0L ($R \approx 1.6$ nm, $l=100$ nm, and $g=2$). (b) Approximation of the previous dependence by $f_i(q_0L)$ ($i=1,\ldots,4$) ($k'L=k''L=0.7$) [see Eqs. (60)–(65)].

$$M_c^+ \propto \int_0^L d\zeta e^{iq_0\zeta} i \cos[k''(L/2-\zeta)] = f_3(q_0L) + if_4(q_0L), \tag{61}$$

$$f_1(q_0L) = \int_0^L d\zeta \cos q_0\zeta \sin[k'(L/2-\zeta)] = 2\frac{-k' \cos\frac{k'L}{2} \sin\frac{q_0L}{2} + q_0 \sin\frac{k'L}{2} \cos\frac{q_0L}{2}}{(k')^2 - q_0^2} \sin\frac{q_0L}{2}, \tag{62}$$

$$f_2(q_0L) = \int_0^L d\zeta \sin q_0\zeta \sin[k'(L/2-\zeta)] = 2\frac{k' \cos\frac{k'L}{2} \sin\frac{q_0L}{2} - q_0 \sin\frac{k'L}{2} \cos\frac{q_0L}{2}}{(k')^2 - q_0^2} \cos\frac{q_0L}{2}, \tag{63}$$

$$f_3(q_0L) = \int_0^L d\zeta \sin q_0\zeta \cos[k''(L/2-\zeta)] = 2\frac{k'' \sin\frac{k''L}{2} \cos\frac{q_0L}{2} - q_0 \cos\frac{k''L}{2} \sin\frac{q_0L}{2}}{(k'')^2 - q_0^2} \sin\frac{q_0L}{2}, \tag{64}$$

$$f_4(q_0L) = -\int_0^L d\zeta \cos q_0\zeta \cos[k''(L/2-\zeta)] = 2\frac{-k'' \sin\frac{k''L}{2} \cos\frac{q_0L}{2} + q_0 \cos\frac{k''L}{2} \sin\frac{q_0L}{2}}{(k'')^2 - q_0^2} \cos\frac{q_0L}{2}. \tag{65}$$

We have plotted the functions $f_i(q_0L)$ [see Fig. 9(b)] in comparison to the real and imaginary parts of $M_{c,d}^+$ [Fig. 9(a)]. There is a good agreement between the corresponding functions (plotted with the same line style) except for the region of $q_0L < 2\pi$ for $f_3(q_0L)$ and $f_4(q_0L)$. From Fig. 9, Eqs. (62) and (63), one can see that $\mathrm{Re}(M_d^+)$ and $\mathrm{Im}(M_d^+)$ have zeroes at $k' \tan q_0L/2 = q_0 \tan k'L/2$ (which are close to $q_0L=(2n+1)\pi$, where $n=1,2,3,\ldots$), in addition, $\mathrm{Re}(M_d^+)$ is zero at $q_0L=2\pi n$ and $\mathrm{Im}(M_d^+)$ is zero at $q_0L=(2n-1)\pi$. From Fig. 9, Eqs. (64) and (65), we get that $\mathrm{Re}(M_c^+)$ and $\mathrm{Im}(M_c^+)$ have zeroes at $k'' \tan k''L/2 = q_0 \tan q_0L/2$ (which are close to $q_0L=2n\pi$), in addition, $\mathrm{Re}(M_c^+)$ is zero at $q_0L=2\pi n$ and $\mathrm{Im}(M_c^+)$ is zero at $q_0L=(2n-1)\pi$. Zeroes of the above functions determine the regions of q_0L in which the sign of those functions is constant, namely,

$$\mathrm{Re}(M_d^+), \quad f_1(q_0L) \lesseqgtr 0 \quad \text{for} \quad 2n\pi \lesseqgtr q_0L \lesseqgtr (2n+1)\pi, \tag{66}$$

$$\mathrm{Re}(M_c^+), \quad f_3(q_0L) > 0 \quad \text{almost for any } q_0L, \tag{67}$$

$$\mathrm{Im}(M_d^+), \quad f_2(q_0L) > 0 \quad \text{almost for any } q_0L > \pi, \tag{68}$$

$$\mathrm{Im}(M_c^+), \quad f_4(q_0L) \lesseqgtr 0 \quad \text{for} \quad 2n\pi \lesseqgtr q_0L \lesseqgtr (2n+1)\pi. \tag{69}$$

From these equations we find that for $2n\pi \lesseqgtr q_0L \lesseqgtr (2n+1)\pi$ the functions $\mathrm{Re}(M_d^+)$ and $\mathrm{Re}(M_c^+)$, as well as, $\mathrm{Im}(M_d^+)$ and $\mathrm{Im}(M_c^+)$ have opposite signs. In other words, *due to odd or even symmetry of vector states with respect to the center of a NT QD* ($\zeta=L/2$), the terms of spin-flip transitions M_d^+ and M_c^+ combine in antiphase at $2n\pi \lesseqgtr q_0L \lesseqgtr (2n+1)\pi$, resulting in destructive interference of those contributions to the spin relaxation rate. Note that $M_{d,c}^-$ terms have similar behavior and the same statements hold true for those. Here $q_0 = \sqrt{\sqrt{2}|\hbar\omega_Z - 2\tau_3\Delta_{\mathrm{curv}}^{\parallel}|}/\hbar c_S R$ is the phonon wave vector of the resonant spin-flip transition. The magnetic-field dependence of q_0 is shown in Fig. 10 (red curve). The regions of q_0L and B, where the destructive interference is expected, are shown by nonshaded areas. From Figs. 4, 5, and 6(a), we see that the destructive interference dips in the spin relaxation rate are in the defined regions shown in Fig. 10.

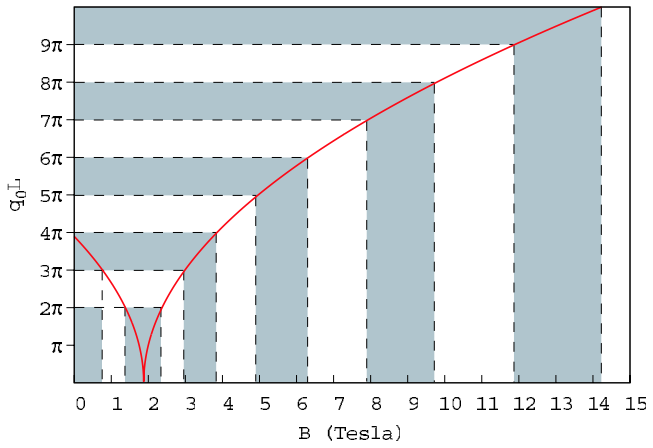

FIG. 10. (Color online) The dependence of $q_0 L$ on magnetic field B ($R \approx 1.6$ nm, $g=2$, and $\Delta_{\mathrm{curv}}^{\parallel}=0.1085$ meV). The nonshaded areas stand for regions of magnetic field where destructive interference occurs.

The effect is stronger for smaller V_g, when the number of discrete levels is lower [see Fig. 6(a)]. In this case, the spin relaxation is predominantly due to coupling to the continuous spectrum. With increasing the voltage V_g applied to top gates, the number of discrete levels and the spacing between the ground state and the lower bound of the continuous spectrum increases. (For instance, in the case of $V_g=2.3$ meV, there are only two discrete levels, while for $V_g=113$ meV, there are about 15 quantized levels in each subband.) This decreases (increases) the contribution of the continuous (discrete) spectrum to the spin relaxation rate and increases the total spin relaxation rate [compare Fig. 5, where $V_g \approx 8.5$ meV, with Fig. 6(a), where $V_g \approx 2.3$ meV for the same type of NT QD]. Such rich and unexpected behavior of the spin relaxation in NT QDs is remarkable and opens up broad perspectives for spintronics in carbon nanostructures.

VII. CONCLUSIONS

In conclusion, contrary to the common belief that spin-orbit interaction is weak and insignificant in carbon materials, we have shown that the situation is actually much richer and that spin-orbit interaction can be very important in nanotubes. We have studied spin relaxation and decoherence caused by electron-lattice and spin-orbit interaction and predict striking nonmonotonic effects induced by magnetic fields B. For particular values of B, destructive interference occurs resulting in ultralong spin relaxation times T_1 exceeding tens of seconds. For small phonon frequencies ω, we find a $1/\sqrt{\omega}$ spin-phonon noise spectrum—a dissipation channel for spins in quantum dots—which can reduce T_1 by many orders of magnitude. We show that nanotubes exhibit zero-field level splitting caused by spin-orbit interaction. This enables an all-electrical and phase-coherent control of spin—the hallmark of spintronics.

ACKNOWLEDGMENTS

We thank G. Burkard, S. Ilani, L. Kouwenhoven, and L. Vandersypen for useful discussions and E. Klinovaya for pointing out several typos. We acknowledge the support from the NSF-CH, NCCR Nanoscience, ONR, and JST ICORP.

APPENDIX A: SPIN SPLITTING AND ELECTRIC-DIPOLE SPIN RESONANCE AT ZERO MAGNETIC FIELDS

From Eq. (36), one can find that there is a zero-field splitting between spin-up and spin-down states,

$$\begin{aligned}(\mathcal{E}_{0,0,1/2} - \mathcal{E}_{0,0,-1/2})|_{B=0} &= \hbar v \sqrt{(-\tau_3 \nu/3R + \Delta_{\mathrm{curv}}^{\parallel}/\hbar v)^2 + k_0^2} \\ &\quad - \hbar v \sqrt{(-\tau_3 \nu/3R - \Delta_{\mathrm{curv}}^{\parallel}/\hbar v)^2 + k_0^2} \\ &\approx -2\tau_3 \nu \Delta_{\mathrm{curv}}^{\parallel}, \end{aligned} \tag{A1}$$

where $\nu=0, \pm 1$, and where we have taken into account that $k_0 \ll 1/R$ and neglected intervalley mixing. Due to the first term in Eq. (34), there is spin mixing and, therefore, coupling between corresponding states [see also Eq. (37)], which allows electric-dipole transitions between them. Consider an oscillating electric field (see Fig. 11): $\mathbf{E}(t) = E\mathbf{e}_{\perp} \sin \omega t$, $\mathbf{e}_{\perp}$ is the unit vector perpendicular to the NT axis. An interaction between the electric field and an electron in a NT, which leads to electric-dipole transitions, is given by the following operator:

$$H_E = \frac{|e|E}{m_0 \omega} \cos \omega t P_{\perp} = \frac{-i|e|\hbar E}{m_0 R \omega} \cos \omega t \sin \varphi \frac{\partial}{\partial \varphi}, \tag{A2}$$

where m_0 is the bare electron mass and $P_{\perp} = -i\hbar \sin \varphi \partial_{\varphi}/R$ is the electron momentum along $\mathbf{e}_{\perp}$. Here we assume that the influence of the lattice potential can be neglected for the estimation of the electric-dipole transitions. Therefore, using Eq. (37), the matrix element of the electric-dipole transitions can be expressed as

$$\begin{aligned}\langle \psi_{0,0,+1/2} | H_E | \psi_{0,0,-1/2} \rangle &= \frac{-i|e|\hbar E}{2m_0 R \omega} \cos \omega t \\ &\quad \times \sum_k \left[(\lambda_k^-)^* \langle \Psi_{\varkappa_{-1}^-, k, -1/2} | ie^{-i\varphi} \frac{\partial}{\partial \varphi} | \Psi_{\varkappa_0^-, k_0, -1/2} \rangle \right. \\ &\quad \left. + \lambda_k^+ \langle \Psi_{\varkappa_0^+, k_0, +1/2} | ie^{-i\varphi} \frac{\partial}{\partial \varphi} | \Psi_{\varkappa_{+1}^+, k, 1/2} \rangle \right] \\ &= \hbar \omega_R \cos \omega t, \end{aligned} \tag{A3}$$

$$\begin{aligned}\omega_R = \frac{i|e|E}{2m_0 R \omega} \sum_k [&(\lambda_k^-)^* \langle \Phi_{\varkappa_{-1}^-, k, -1/2} | \Phi_{\varkappa_0^-, k_0, -1/2} \rangle \\ &+ \lambda_k^+ \langle \Phi_{\varkappa_0^+, k_0, +1/2} | \Phi_{\varkappa_{+1}^+, k, 1/2} \rangle]. \end{aligned} \tag{A4}$$

Here the sum includes summation over the discrete k_n and integration over the continuous $|k| \geq (|V_g|/\hbar v)\sqrt{1 + 2\hbar v |\kappa_m|/V_g}$. Numerical evaluation leads to the following estimates for the resonance frequency $\omega = 2\Delta_{\mathrm{curv}}^{\parallel}/\hbar \approx 33 \times 10^{10}$ s^{-1} ($\Delta_{\mathrm{curv}}^{\parallel} \approx 0.11$ meV) and Rabi frequency $\omega_R \approx 1.6 \times 10^5$ s^{-1} at $E=10$ V/cm and $V_g = 2.3$ meV.

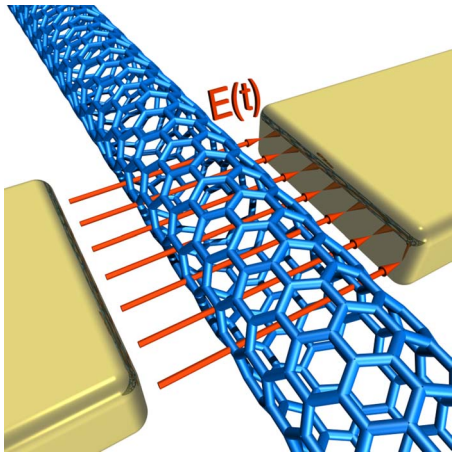

FIG. 11. (Color online) Scheme of a NT with two electric side gates. An applied ac voltage between the gates creates an oscillating electric field perpendicular to the NT axis. Such a setup enables electrically induced coherent spin manipulation, due to zero-field spin splitting in semiconducting NTs.

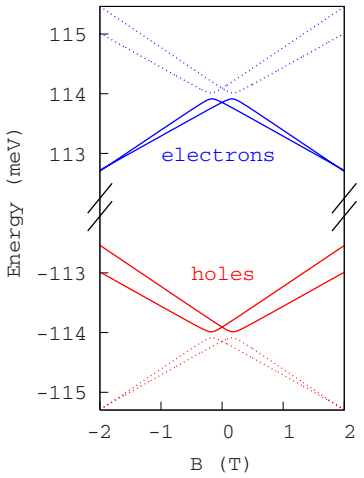

FIG. 12. (Color online) Magnetic field dependence of energy levels for electrons (blue curves) and holes (red curves). The dashed curves are the excited states in a NT QD ($R \approx 1.6$ nm, $L=100$ nm, $g=2$, and $V_g \approx \pm 8.5$ meV [the upper (lower) sign is for electrons (holes)], $\Delta_{\mathrm{curv}}^{\parallel}=0.11$ meV, and $\Delta_{\mathbf{K}-\mathbf{K}'}=0.05$ meV).

APPENDIX B: VALLEY-ORBIT AND SPIN-ORBIT INTERACTIONS

In this appendix, we consider a particle in a NT described by the Hamiltonian (3) with the longitudinal confinement (9) in a parallel magnetic field. The discrete spectrum of a such system is given by

$$E_{m,n,S_\zeta} = \pm \hbar v \sqrt{\kappa_m^2 + k_n^2} + S_\zeta \hbar \omega_Z, \tag{B1}$$

where $\kappa_m=(m-\tau_3\nu/3+\varphi_{\mathrm{AB}})/R$ and $\varphi_{\mathrm{AB}}=\Phi_{\mathrm{AB}}/\Phi_0$. Each level is fourfold degenerate (at $B=0$) due to valley and spin degeneracy. Now, we take SOI into account. For definiteness, we consider only the second term in Eq. (34) which leads to zero-field splitting,

$$H_{\mathrm{SO}}^{\mathrm{curv}} = \Delta_{\mathrm{curv}}^{\parallel} \tau_3 \sigma_1 2 S_\zeta. \tag{B2}$$

Moreover, within a minimal model we take intervalley mixing due to nonmagnetic impurities or structure defects into account. In this case, the intervalley mixing can be described by the following term:

$$H_{\mathbf{K}-\mathbf{K}'} = \Delta_{\mathbf{K}-\mathbf{K}'} \tau_1, \tag{B3}$$

where τ_1 is the Pauli matrix operating on valley-index space. The eigenvalues of the operator $H_0+V(\zeta)+H_{\mathrm{SO}}^{\mathrm{curv}}+H_{\mathbf{K}-\mathbf{K}'}$ (for $m=0$ subband) are given by

$$\begin{aligned} E_{0,n,S_\zeta} &= \pm \hbar v [\nu^2/9R^2 + k_n^2 + k_{\mathbf{K}-\mathbf{K}'}^2 + (\varphi_{\mathrm{AB}}/R + 2S_\zeta k_{\mathrm{SO}})^2 + 2\beta \\ &\times \sqrt{(\varphi_{\mathrm{AB}}/R + 2S_\zeta k_{\mathrm{SO}})^2 \nu^2/9R^2 + k_{\mathbf{K}-\mathbf{K}'}^2 (\nu^2/9R^2 + k_n^2)}]^{1/2} \\ &+ S_\zeta \hbar \omega_Z, \end{aligned} \tag{B4}$$

where $k_{\mathbf{K}-\mathbf{K}'}=\Delta_{\mathbf{K}-\mathbf{K}'}/\hbar v$ and $k_{\mathrm{SO}}=\Delta_{\mathrm{curv}}^{\parallel}/\hbar v$. The energy spectrum of the lowest electron energy levels and highest hole levels described by Eq. (B4) is shown in Fig. 12 ($n=0$). In Eq. (B4), the plus (minus) sign corresponds to electron (hole) energy levels. $\beta=1$ for the upper branch of the energy spectrum (blue dashed and red solid curves) and $\beta=-1$ for the lower branch (blue solid and red dashed curves). Using $|\kappa_m| \gg k_n$, we rewrite Eq. (B4) in the following way:

$$\begin{aligned} E_{0,n,S_\zeta} &= \pm \hbar v \sqrt{\nu^2/9R^2 + k_n^2} \\ &+ \beta \hbar v \sqrt{k_{\mathbf{K}-\mathbf{K}'}^2 + (\varphi_{\mathrm{AB}}/R + 2S_\zeta k_{\mathrm{SO}})^2} + S_\zeta \hbar \omega_Z \\ &+ O(3\nu k_n R \varphi_{\mathrm{AB}}). \end{aligned} \tag{B5}$$

From this equation we find that the zero-field splitting of levels is given by $\hbar v \sqrt{k_{\mathrm{SO}}^2 + k_{\mathbf{K}-\mathbf{K}'}^2}$ and anticrossings (with the magnitude $2|\Delta_{\mathbf{K}-\mathbf{K}'}|$) occur at $\varphi_{\mathrm{AB}}=-2S_\zeta k_{\mathrm{SO}} R=0$.

Due to intervalley coupling, electron states of different nonequivalent $\mathbf{K}$ points are mixed,

$$\Psi_{\mathbf{K}} \approx \Psi_{\mathbf{K}}^{(0)} + \frac{\Delta_{\mathbf{K}-\mathbf{K}'}}{\sqrt{\Delta_{\mathbf{K}-\mathbf{K}'}^2 + (\hbar v \varphi_{\mathrm{AB}}/R + 2S_\sigma \Delta_{\mathrm{curv}}^{\parallel})^2}} \Psi_{\mathbf{K}'}^{(0)}. \tag{B6}$$

The mixing is maximal at the anticrossing points (at that point, the electron state is just a superposition of those corresponding to different $\mathbf{K}$ points) and suppressed away from them. Therefore, there is a way to control the intervalley mixing for a NT by a magnetic field and it makes NTs attractive for a valley-qubit realization (qubits whose quantum states are defined by the valley index).[22,38,39]

At anticrossing points, mixing of $\mathbf{K}$ and K' valleys is strong and intervalley scattering could occur. Note that such scattering is energetically forbidden for first-order processes (with one-phonon scattering). Indeed, scattering from $\mathbf{K}$ to $\mathbf{K}'$ point requires a large change in the electron wave vector ($|\mathbf{K}-\mathbf{K}'|=|\mathbf{K}|$), while the energy difference between the scattering states is small ($2\Delta_{\mathbf{K}-\mathbf{K}'} \leq 0.5$ meV). Phonons in a NT at the $\mathbf{K}$ point of the phonon dispersion have much higher energy ($\omega_K > 600$ cm^{-1} which correspond to 75 meV),[40] and

therefore, first-order single-phonon intervalley scattering is forbidden. However, Raman spectroscopy has shown that such an intervalley scattering is allowed for photoexcited electrons. Such transitions are attributed to second-order Raman processes by two phonon emission or emission of one phonon and elastic scattering on lattice defects (so-called D and G' bands in the Raman spectra).[40] We assume that similar processes could occur in our case, due to spontaneous phonon emission and absorption with $\hbar\omega_1 - \hbar\omega_2 = 2\Delta_{\mathbf{K}-\mathbf{K}'}$ and $\mathbf{q}_1 - \mathbf{q}_2 = \mathbf{K}$ or to emission of a single phonon with $\mathbf{q} = \mathbf{K}$ and elastic scattering on lattice defects but are nevertheless less probable.

[1] D. D. Awschalom and M. E. Flatté, Nat. Phys. **3**, 153 (2007).
[2] S. Sahoo, T. Kontos, J. Furer, C. Hoffmann, M. Gräber, A. Cottet, and C. Schönenberger, Nat. Phys. **1**, 99 (2005).
[3] N. Tombros, S. J. van der Molen, and B. J. van Wees, Phys. Rev. B **73**, 233403 (2006).
[4] T. Ando, J. Phys. Soc. Jpn. **74**, 777 (2005).
[5] A. K. Geim and K. S. Novoselov, Nat. Mater. **6**, 183 (2007).
[6] H. Min, J. E. Hill, N. A. Sinitsyn, B. R. Sahu, L. Kleinman, and A. H. MacDonald, Phys. Rev. B **74**, 165310 (2006).
[7] D. Loss and D. P. DiVincenzo, Phys. Rev. A **57**, 120 (1998).
[8] A. V. Khaetskii and Y. V. Nazarov, Phys. Rev. B **61**, 12639 (2000).
[9] V. N. Golovach, A. Khaetskii, and D. Loss, Phys. Rev. Lett. **93**, 016601 (2004).
[10] D. V. Bulaev and D. Loss, Phys. Rev. B **71**, 205324 (2005).
[11] S. J. Tans, M. H. Devoret, H. Dai, A. Thess, R. E. Smalley, L. J. Geerligs, and C. Dekker, Nature (London) **386**, 474 (1997).
[12] M. Bockrath, W. Liang, D. Bozovic, J. H. Hafner, Ch. M. Lieber, M. Tinkham, and H. Park, Science **275**, 1922 (1997).
[13] J. Kong, C. Zhou, E. Yenilmez, and H. Dai, Appl. Phys. Lett. **77**, 3977 (2000).
[14] E.D. Minot, Y. Yaish, V. Sazonova, and P. L. McEuen, Nature (London) **428**, 536 (2004).
[15] P. Jarillo-Herrero, S. Sapmaz, C. Dekker, L. P. Kouwenhoven, and H. S. J. van der Zant, Nature (London) **429**, 389 (2004).
[16] N. Mason, M. J. Biercuk, and C. M. Marcus, Science **303**, 655 (2004).
[17] S. Sapmaz, C. Meyer, P. Beliczynski, P. Jarillo-Herrero, and L. P. Kouwenhoven, Nano Lett. **6**, 1350 (2006).
[18] M. R. Gräber, W. A. Coish, C. Hoffmann, M. Weiss, J. Furer, S. Oberholzer, D. Loss, and C. Schönenberger, Phys. Rev. B **74**, 075427 (2006).
[19] D. P. DiVincenzo and E. J. Mele, Phys. Rev. B **29**, 1685 (1984).
[20] S. G. Lemay, J. W. Janssen, M. van den Hout, M. Mooij, M. J. Bronikowski, P. A. Willis, R. E. Smalley, L. P. Kouwenhoven, and C. Dekker, Nature (London) **412**, 617 (2001).
[21] M. I. Katsnelson, K. S. Novoselov, and A. K. Geim, Nat. Phys. **2**, 620 (2006).
[22] B. Trauzettel, D. V. Bulaev, D. Loss, and G. Burkard, Nat. Phys. **3**, 192 (2007).
[23] W. Liang, M. Bockrath, D. Bozovic, J. H. Hafner, M. Tinkham, and H. Park, Nature (London) **411**, 665 (2001).
[24] K. Grove-Rasmussen, H. I. Jorgensen, and P. E. Lindelof, Physica E (Amsterdam) **40**, 92 (2007).
[25] L. G. Herrmann, T. Delattre, P. Morfin, J.-M. Berroir, B. Placais, D. C. Glattli, and T. Kontos, Phys. Rev. Lett. **99**, 156804 (2007).
[26] C. L. Kane and E. J. Mele, Phys. Rev. Lett. **95**, 226801 (2005).
[27] D. Huertas-Hernando, F. Guinea, and A. Brataas, Phys. Rev. B **74**, 155426 (2006).
[28] T. Ando, J. Phys. Soc. Jpn. **69**, 1757 (2000).
[29] M. Willatzen, M. Cardona, and N. E. Christensen, Phys. Rev. B **50**, 18054 (1994).
[30] D. Tomanek and S. G. Louie, Phys. Rev. B **37**, 8327 (1988).
[31] F. Kuemmeth, S. Ilani, D. Ralph, and P. L. McEuen, Nature (London) **452**, 448 (2008).
[32] P. Jarillo-Herrero, J. Kong, H. S. J. van der Zant, C. Dekker, L. P. Kouwenhoven, and S. De Franceschi, Phys. Rev. Lett. **94**, 156802 (2005).
[33] R. Saito, G. Dresselhaus, and M. S. Dresselhaus, *Physical Properties of Carbon Nanotubes* (Imperial College, London, 1999).
[34] J. Maultzsch, H. Telg, S. Reich, and C. Thomsen, Phys. Rev. B **72**, 205438 (2005).
[35] S. V. Goupalov, Phys. Rev. B **71**, 085420 (2005).
[36] H. Suzuura and T. Ando, Phys. Rev. B **65**, 235412 (2002).
[37] K. Blum, *Density Matrix Theory and Applications* (Plenum, New York, 1996).
[38] P. Recher, B. Trauzettel, A. Rycerz, Ya. M. Blanter, C. W. J. Beenakker, and A. F. Morpurgo, Phys. Rev. B **76**, 235404 (2007).
[39] A. Rycerz, J. Tworzydlo, and C. W. J. Beenakker, Nat. Phys. **3**, 172 (2007).
[40] R. Saito, A. Grüneis, Ge. G. Samsonidze, V. W. Brar, G. Dresselhaus, M. S. Dresselhaus, A. Jorio, L. G. Cançado, C. Fantini, M. A. Pimenta, and A. G. Souza Filho, New J. Phys. **5**, 157 (2003).